

# Enhanced irradiation tolerance of Fe<sub>30</sub>Cr<sub>25</sub>Ni<sub>20</sub>Co<sub>15</sub>Mn<sub>10</sub> high-entropy alloy via nanotwin boundaries

Y. Zhang<sup>a</sup>, W.Q. Jiang<sup>a</sup>, A. Gokhman<sup>b</sup>, J.J. Yang<sup>c</sup>, K. Shi<sup>c</sup>, J.H. Luan<sup>d</sup>, Y. Cui<sup>a,\*</sup>, Peter K Liaw<sup>e</sup>, C.T. Liu<sup>d</sup>, Z.W. Zhang<sup>a,f,\*</sup>

<sup>a</sup> Key Laboratory of Superlight Materials and Surface Technology, Ministry of Education, College of Materials Science and Chemical Engineering, Harbin Engineering University, No.145, Nantong Street, Harbin 150001, China

<sup>b</sup> Department of Physics, South Ukrainian National Pedagogical University, Odessa 65020, Ukraine

<sup>c</sup> Key Laboratory of Radiation Physics and Technology of Ministry of Education, Institute of Nuclear Science and Technology, Sichuan University, Chengdu 610064, China

<sup>d</sup> Department of Materials Science Engineering, College of Science and Engineering, City University of Hong Kong, China

<sup>e</sup> Department of Materials Science and Engineering, The University of Tennessee, Knoxville, TN 37996-2100, USA

<sup>f</sup> State Key Laboratory of Metal Material for Marine Equipment and Application, Iron & Steel Research Institute of Ansteel Group Corporation, Anshan, Liaoning 114009, China

## ARTICLE INFO

### Article history:

Received 19 June 2021

Revised 14 August 2021

Accepted 7 September 2021

Available online 9 September 2021

### Keywords:

High-entropy alloy

Irradiation resistance

Twin boundary

Irradiation-induced swelling

## ABSTRACT

High-entropy alloys (HEAs) have been considered as a promising candidate for nuclear engineering due to their intriguing irradiation tolerance. The microstructure stabilities, including the radiation-induced precipitation (RIP), swelling, and segregation (RIS) in HEAs, are of great significance for applications. In this paper, the Fe<sub>30</sub>Cr<sub>25</sub>Ni<sub>20</sub>Co<sub>15</sub>Mn<sub>10</sub> HEA was irradiated by high-energy Au<sup>2+</sup> ions with a peak dose of ~ 70 displacements per atom (dpa). The formation of voids, nanoscale precipitation, segregation, and mechanical properties before and after irradiation was characterized carefully, using scanning/transmission electron microscopy (S/TEM), atom probe tomography (APT), and nanoindentation. The results indicate that the HEA presents a very low swelling rate of ~ 0.002%/dpa. After irradiation, no nanoscale precipitation is observed, confirming the excellent stability of the HEA microstructure. The RIS is observed for the first time at nanotwin boundaries in the HEA after irradiation. The elements, Co and Ni, are enriched slightly, while Fe, Cr, and Mn depleted on the nanotwin boundaries after irradiation. The irradiation-induced segregation level is obviously suppressed in the HEA due to the sluggish atom diffusion. The hardness remains almost unchanged after irradiation. The nanotwin boundaries act as defect sinks to absorb irradiation-induced vacancies and interstitials, reducing the swelling rate and relieving hardening. The low swelling, weak RIS level, and almost no hardening after a high dose irradiation indicate that the Fe<sub>30</sub>Cr<sub>25</sub>Ni<sub>20</sub>Co<sub>15</sub>Mn<sub>10</sub> HEA possesses an outstanding irradiation tolerance.

© 2021 Elsevier B.V. All rights reserved.

## 1. Introduction

The development of next-generation fission and fusion reactors requires advanced structural materials possessing good microstructure stability and excellent radiation tolerance under extreme environments, such as the high irradiation dose and elevated temperatures [1,2]. High-entropy alloys (HEAs) have attracted a great interest due to their excellent properties, such as great mechanical

properties, high irradiation and corrosion resistance, which make them good candidates for core components in next-generation nuclear reactors [3–8]. Recent studies have shown that HEAs exhibit an excellent radiation tolerance, as compared to the traditional nuclear materials, since their alloy complexity reduces defect mobility and alters migration paths on a modified energy landscape, altering defect dynamics to promote defects annihilation and ultimately enhancing radiation resistance [2,9–13].

Precipitation and phase separation may occur under irradiation due to the compositional complexity of HEAs, inducing the structure and composition change, which may reduce the performances (e.g., swelling and embrittlement) [14]. Therefore, the composition and structure stabilities of HEAs under irradiation are critical for the applications as nuclear materials. The solute redistribution at defect sinks induced by irradiation is generally referred to as the

\* Corresponding authors at: Key Laboratory of Superlight Materials and Surface Technology, Ministry of Education, College of Materials Science and Chemical Engineering, Harbin Engineering University, No.145, Nantong Street, Harbin 150001, China.

E-mail addresses: [cuiye@hrbeu.edu.cn](mailto:cuiye@hrbeu.edu.cn) (Y. Cui), [zwzhang@hrbeu.edu.cn](mailto:zwzhang@hrbeu.edu.cn) (Z.W. Zhang).

radiation-induced segregation (RIS). When the content of segregated solute atoms at a sink reaches the limit of solubility in the alloy, a new phase can nucleate and grow, leading to the radiation-induced precipitation (RIP) [15]. Since the mid-seventies, many RIS and RIP phenomena have been reported in structural materials of nuclear reactors or model alloys [16–19]. In general, the former is considered as one of the main factors to irradiation-assisted stress corrosion cracking (IASCC) [20], and the latter leads to the hardening and embrittlement of materials. For example, the RIS of Cr at grain boundaries in austenitic stainless steels results in the occurrence of IASCC [20]. The hardening and embrittlement of pressure vessel steels are generally attributed to the RIP of Cu-rich nanoclusters [21–24]. However, there are not sufficient experimental studies on the irradiation behaviors in HEAs. Lu et al. report the RIS behaviors of NiFe, NiCoFe, NiCoFeCr, and NiCoFeCrMn on dislocation loops and voids, and they find that the RIS level is greatly reduced by increasing the compositional complexity [25]. The equiatomic CoCrFeNiMn HEA exhibits the enhanced radiation tolerance and suppression of the formation of voids under the Ni-ion irradiation [26]. But the significant Mn depletion and Co and Ni enrichment at grain boundaries are observed.

It is known that twin boundaries, grain boundaries, and pre-existing precipitates all can act as defect traps enhancing the irradiation tolerance, such as reducing the swelling rate/hardening and preventing RIP [27–29]. A large number of studies focus on the grain boundaries and pre-existing precipitates. Twin boundaries are more stable than other common interfaces [30]. Meric de Bellefont et al. found that swelling can be suppressed in regions containing a high density of closely-spaced deformation twin boundaries in a nanotwinned austenitic stainless steel [27]. Both coherent and incoherent twin boundaries are critical to remove some of the most stable defect clusters (SFTs) induced and defect loops by radiation in nanotwinned Ag, improving radiation-tolerant properties [31,32]. However, to our knowledge, there are very few reports on the effects of twin boundaries on the irradiation tolerance, especially in HEAs. It is known that face-centered-cubic (FCC) HEAs possess extreme-low stacking fault energies and thus, are easy to form twins [33]. Therefore, it is vital to understand the effects of nanotwin boundaries on the swelling, RIP, and RIS in HEAs to develop irradiation-tolerant HEAs.

It is reported that the equivalent FeCrNiCoMn HEA can provide a good irradiation resistance [11,12,34]. The FeCrNiCoMn system possesses the low stacking fault energy (SFE, 21 mJ/m<sup>2</sup>) [35], and a high density of twins after dynamic recrystallization [36,37]. He et al. proposed a criterion that when all elemental pairs satisfy  $-7 \text{ kJ/mol} \leq \Delta H_{\text{mix}} \leq 0$  (for example, FeCrNiCo without Mn), the alloy microstructure remains stable up to 1 dpa [34]. In addition, previous studies indicate that Fe doping in Ni can greatly delay the defect evolution [38] and decrease the swelling [39]. In this paper, starting from the equivalent FeCrNiCoMn system, the content of Fe is increased to delay the defect evolution and decrease the swelling. In order to balance the increase in Fe, the content of Mn is reduced. For Fe-Mn-based systems, when the Mn content is from 16 at.% to 33 at.%, the decrease in Mn decreases SFE by 18 mJ/m<sup>2</sup> per 1 at.% Mn [40–42]. The reduction in Mn can also retain the low SFE, benefiting to the formation of twins. Thus, a novel HEA with the optimized composition of a non-equivalent Fe<sub>30</sub>Cr<sub>25</sub>Ni<sub>20</sub>Co<sub>15</sub>Mn<sub>10</sub> is developed. By this way of the composition design, a high density of nanotwins can be obtained to investigate the role of nanotwin boundaries on the irradiation tolerance. Most of the previous studies mainly focused on the high temperature and low doses (< 10 dpa) irradiation [34,43,44]. However, the irradiation responses of HEAs at high temperatures and low doses are drastically different from those at room temperature and high doses ( $\geq 10$  dpa) [14]. Thus, in order to exclude the effect of temperature, here we irradiated the HEA to

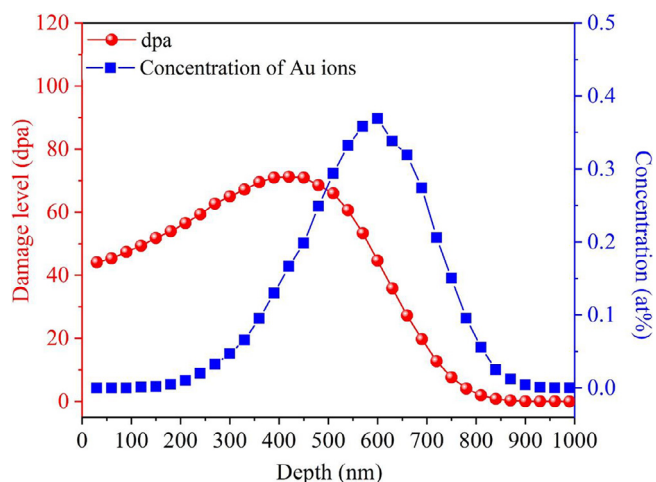


Fig. 1. The profiles of the damage (dpa) and distribution of the Au<sup>2+</sup> ions along the depth calculated by SRIM for the Fe<sub>30</sub>Cr<sub>25</sub>Ni<sub>20</sub>Co<sub>15</sub>Mn<sub>10</sub> HEA.

a high dose of  $\sim 70$  dpa at room temperature using heavy ions to trace the microstructure evolution. The microstructure evolution, RIP, and RIS in the newly-developed Fe<sub>30</sub>Cr<sub>25</sub>Ni<sub>20</sub>Co<sub>15</sub>Mn<sub>10</sub> HEA are studied by the nanoindentation, atom probe tomography (APT), and scanning/transmission electron microscopy (S/TEM). The special attention is paid to the estimation of the sink strengths of different types of sinks for defects induced by ion irradiation. The mechanisms for the enhanced irradiation tolerance of the Fe<sub>30</sub>Cr<sub>25</sub>Ni<sub>20</sub>Co<sub>15</sub>Mn<sub>10</sub> alloy under high doses of heavy ion irradiation are discussed in detail.

## 2. Experimental

The Fe<sub>30</sub>Cr<sub>25</sub>Ni<sub>20</sub>Co<sub>15</sub>Mn<sub>10</sub> HEA was prepared, using high vacuum arc melting with high-purity (> 99.9%, weight percent) raw materials and drop-cast into a  $\phi 20$  mm water-cooled copper mold. The as-cast ingots were homogenized at 1200 °C for 1 h, followed by water quenching. The as-quenched samples were then cold rolled to an 80% thickness reduction to introduce a large amount of nanotwins. The as-rolled samples were then annealed at 1000 °C for 1 h.

The microstructure for the un-irradiated sample was observed, using the Electron Back-scattered Diffraction (EBSD) on a Hitachi S3400 scanning electron microscope equipped with the HKL Channel 5 software [45]. X-ray diffraction (XRD) was conducted on a RIGAKU diffractometer (Panalytical Empyrean) equipped with Cu K $\alpha$  radiation. The Williamson-Hall method was used to measure the dislocation density from the XRD data [46,47].

The Au<sup>2+</sup>-ion irradiation was conducted in the accelerator-ion facilities of the Sichuan University. The prepared HEA samples ( $3 \times 7 \times 0.4$  mm<sup>3</sup>) were irradiated by 6 MeV Au<sup>2+</sup> at a fluence of  $1 \times 10^{16}$  ion/cm<sup>2</sup>. The dose rate is 0.006 dpa/s. The irradiation was performed at  $51 \pm 10$  °C. The profiles of the damage rate in dpa and distribution of the implanted Au<sup>2+</sup> ion were calculated on the Stopping and Range of Ions in Matter (SRIM 2008) [48]. Full Damage Cascade model is used for the SRIM calculation. The displacement threshold energy  $E_d$  for Fe, Cr, Ni, Co and Mn elements is all 40 eV [49,50]. After irradiation, the obtained peak dose was  $\sim 70$  dpa at about 400 nm along the depth as shown in Fig. 1.

Three-dimensional APT was conducted to investigate the RIP behavior. APT was performed, using the CAMECA LEAP 5000 R in a high-voltage electric pulse mode. The data is collected at a temperature of 60 K, and the pulse frequency and pulse ratio are 200 kHz and 20%, respectively. An evaporation detection rate of 0.1% atom per pulse for the voltage pulse mode was used. The

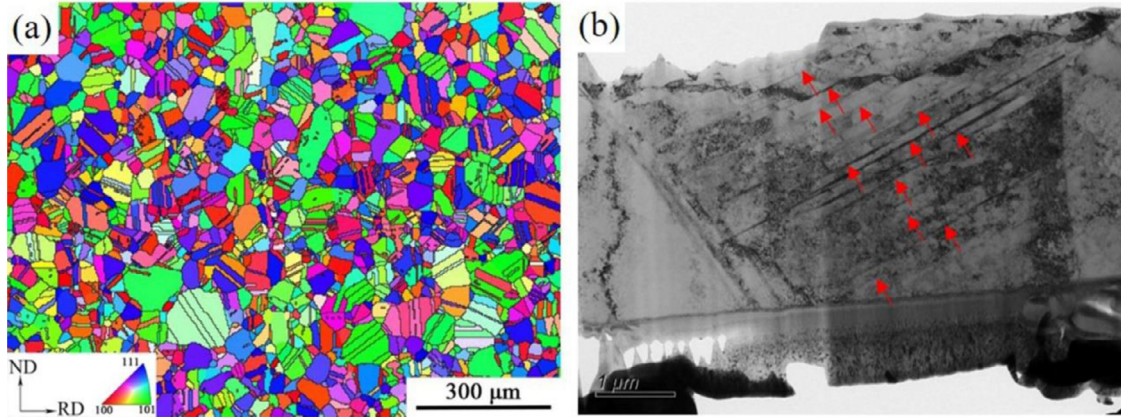


**Fig. 2.** (a) Typical microstructure of the annealed Fe<sub>30</sub>Cr<sub>25</sub>Ni<sub>20</sub>Co<sub>15</sub>Mn<sub>10</sub> alloy, showing a large number of annealing twins, (b) the bright-field TEM image from the FIB sample, showing plenty of nanotwins (red arrows) (For interpretation of the references to color in this figure legend, the reader is referred to the web version of this article).

needle-shaped specimen for APT was prepared at the required positions from the implanted surface by annular milling in a FEI Nova 200 focused ion beam/scanning electron microscope (FIB/SEM). Imago Visualization and Analysis Software version 3.8 was used for creating the 3D reconstructions and data analysis [20]. As all the elements distribute uniformly, isoconcentration surfaces are not used in the reconstruction of APT.

The microstructure evolution and RIS were studied by TEM and energy dispersive x-ray spectroscopy (EDS) in a STEM (FEI Talos F200). Cross-sectional TEM specimens along the depth direction from the irradiated surface were prepared by the Focused Ion Beam (FIB) method using the conventional lift-out technique. The thickness of TEM sample was measured by convergent-beam electron diffraction (CBED). An un-irradiated control sample was also prepared with the same method. RIS on twin boundaries were characterized, using the STEM bright-field EDS line scanning [51]. Nanoindentation tests were conducted on an Agilent Nano Indenter G200 with a Berkovich diamond tip to trace the hardness variations before and after ion irradiation. At least ten points for each sample were taken to obtain an average value.

### 3. Results

#### 3.1. The microstructure and phase components before irradiation

The typical microstructure of the annealed Fe<sub>30</sub>Cr<sub>25</sub>Ni<sub>20</sub>Co<sub>15</sub>Mn<sub>10</sub> alloy is shown in Fig. 2a. A completely-recrystallized microstructure along with a large number of annealing twins can be observed, indicating that the SFE of this HEA system is low enough. The mean grain size ( $d_g$ ) is determined by a linear intercept method as  $\sim 42 \mu\text{m}$  with a standard deviation of  $26 \mu\text{m}$ . The substructure was characterized by TEM to observe the nanotwins, as presented in Fig. 2b. It is obvious that there are two sets of twins in the alloy, annealing twins with a large size and nanotwins. The thickness of twins,  $d_t$ , can be expressed as [52]

$$d_t = ql \quad (1)$$

where  $q$  is an aspect ratio, and  $l$  is the twin length.  $q$  and  $l$  are described as follows [53]:

$$q \cong 0.53 - \frac{1}{2N_L} \sqrt{1.14N_L^2 - \frac{\pi}{2}N_A V_V} \quad (2)$$

$$l \cong \frac{8N_L}{\pi N_A} \left( \frac{\pi}{4} - 0.36q \right) \quad (3)$$

where  $N_L$  is the number of twins intercepting a line of unit length,  $N_A$  is the number of twins per unit area, and  $V_V$  is the volume

fraction of twins. The areal fractions of twins are measured, employing a point counting analysis with a rectangular net, which is assumed to be equivalent to the volume fraction ( $V_V$ ) [54,55]. For the large-size annealing twins,  $N_L = 15.33 \text{ mm}^{-1}$ ,  $N_A = 469 \text{ mm}^{-2}$ ,  $V_V = 0.22$ , and  $d_t = 11.64 \mu\text{m}$  can be obtained. For nanotwins,  $N_L = 2.39 \times 10^3 \text{ mm}^{-1}$ ,  $N_A = 5.45 \times 10^7 \text{ mm}^{-2}$ ,  $V_V = 0.069$ , and  $d_t = 28 \text{ nm}$  can be obtained.

The mean number of twins per grain,  $N_G$ , can be described as [53]

$$N_G = \frac{N_V}{N'_V} = \frac{N_A d^3}{0.57lk(q)} \quad (4)$$

where  $d$  is the linear intercept grain size ( $0.053 \text{ mm}$  for both annealing and nanotwins), and  $k(q)$  is a geometrical function of the aspect ratio [53].

$$k(q) = \frac{1}{2} \left[ q + \frac{\sin^{-1} \sqrt{1-q^2}}{\sqrt{1-q^2}} \right], \text{ for } q < 4, k(q) \cong 0.12q + \frac{\pi}{4} \quad (5)$$

Thus, the number of twins per grain,  $N_G$ , can be estimated as  $2.5$  and  $2.36 \times 10^8$  per grain for annealing and nanotwins, respectively. It is very clear that the number density of nanotwins is far higher than that of annealing twins. Therefore, the nanotwin boundaries can play the main role in the defects absorption compared to the annealing twins. The total volume of nanotwins in a single grain ( $V_t$ ) and the volume of single grain ( $V_g$ ) are calculated. The nanotwins are assumed to be oblate spheroids. Therefore, the nanotwin and the grain can be treated as oblate cylinder and sphere while calculating their volume. The grain size ( $d$ ), nanotwin thickness ( $d_t$ ), aspect ratio ( $q$ ) and the number of twins per grain ( $N_G$ ) are  $53 \mu\text{m}$ ,  $27 \text{ nm}$ ,  $0.36$  and  $2.36 \times 10^8$ , respectively.  $V_t$  and  $V_g$  can be calculated using following equations:

$$V_t = \pi d_t N_G \left( \frac{d_t/q}{2} \right)^2 \quad (6)$$

$$V_g = \frac{4}{3} \pi \left( \frac{d}{2} \right)^3 \quad (7)$$

Thus, the  $V_t$  and  $V_g$  can be estimated as  $2.8 \times 10^{-14}$  and  $7.8 \times 10^{-14} \text{ m}^3$ . The results show that the total volume of nanotwins in a single grain is obviously smaller than that of single grain. Considering the error of statistical results, these conclusions seem to be reasonable.

The X-ray patterns from the as-cast and annealed Fe<sub>30</sub>Cr<sub>25</sub>Ni<sub>20</sub>Co<sub>15</sub>Mn<sub>10</sub> are presented in Fig. 3. Only FCC peaks are identified in both samples, showing that the Fe<sub>30</sub>Cr<sub>25</sub>Ni<sub>20</sub>Co<sub>15</sub>Mn<sub>10</sub>



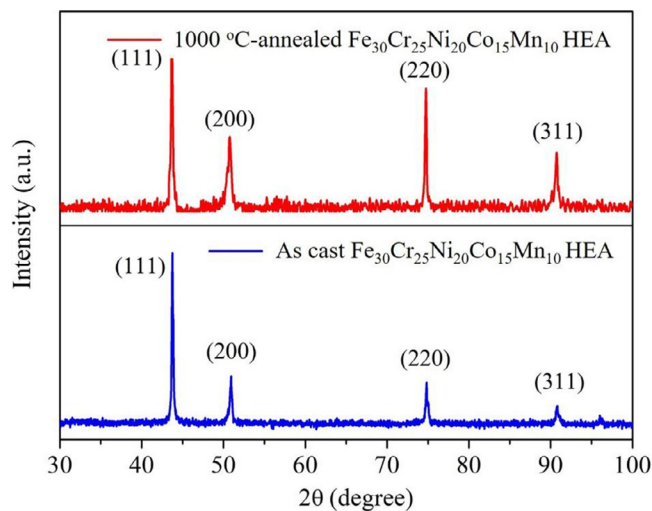


Fig. 3. XRD patterns of the as-cast and annealed  $\text{Fe}_{30}\text{Cr}_{25}\text{Ni}_{20}\text{Co}_{15}\text{Mn}_{10}$  HEA.

HEA exhibits the single FCC phase. The dislocation density,  $\rho_d$ , is estimated roughly to be  $4.56 \times 10^{13} \text{ m}^{-2}$  in 1000 °C-annealed samples based on the XRD result.

### 3.2. Formation of voids in the HEA upon $\text{Au}^{2+}$ ion irradiation

To investigate the microstructure and the formation of irradiation-induced voids along the depth of the irradiation direction, the microstructure from the surface down to the depth of  $\sim 3750 \text{ nm}$  was characterized, as presented in Fig. 4a. The corresponding selected area diffraction (SAED) pattern inserted in Fig. 4b shows two sets of diffraction spots, demonstrating the existence of twin structures.

The higher-magnification micrographs of voids in the corresponding white regions of Fig. 4a are shown in Fig. 4c and d. The bright-field (BF) TEM on both under- (white dot) and over-focused (black dot) modes was performed [44], and a large number of small voids was observed. The diameters of voids span from 3 to 8 nm, and a mean size of  $\sim 5 \text{ nm}$  can be estimated. The voids mainly distribute between 500 and 2500 nm in depth from the surface, and there are almost no voids over 3000 nm. It should be noted that the dose peak locates at around 400 nm in depth from the surface (SRIM results in Fig. 1). This trend indicates that the formation locations of the voids do not match with the dose-peak position. The number density of voids in Fig. 4c is obviously lower than that in Fig. 4d, indicating that most of the voids form behind the dose peak.

In the early studies, it is verified that high entropy alloys possess the slow diffusion effect by interdiffusion experiments with the Darken manning formalism for analysis, quasi-binary approach, and theoretical calculations [56]. The effective diffusion rate of atoms in HEAs is seriously affected by the interaction between different atoms and the lattice distortion. The slow diffusion in HEAs is attributed to the large lattice potential energy fluctuation, which produces more significant atomic traps and blocks, resulting in the higher activation energy of diffusion [57]. However, the slow diffusion of elements cannot be observed directly in some HEAs in recent studies [58]. But for both sides of supporting the sluggish diffusion in HEAs or not, it is accepted that the complexity of lattice structures plays a more important role in diffusion in HEAs [59]. In traditional alloys, interstitial atoms diffuse fast and vacancies diffuse slowly. Vacancies retain after interstitial atoms migrating and then aggregate to form voids. However, due to the existence of large lattice distortion in high-entropy alloys, it may limit the interstitial atom diffusion, and help the diffusion of vacancies,

leading to the opposite phenomenon from the traditional alloys: in high-entropy alloys, the diffusion of vacancies may be fast and the diffusion of interstitial atoms may be slow, causing the formation of voids to deviate from the results of SRIM calculations. This phenomenon was also observed in Ni-20Fe/Cr/Mn/Pd [60], NiCoFe [12], FeCrNiCoMn [12,50], and NiCoFeCrPd [50,61]. Most of the interstitial clusters in HEAs were immobile and retained within the defect-production region, resulting in a high defect recombination rate in this region. Molecular dynamics simulations of one-dimensional (1D) and 3D motions of interstitial clusters under ion irradiation show that only the vacancies that escaped from the cascade-formation range may agglomerate into voids in the deeper regions, while most vacancies are likely annihilated by interstitials in the shallow region [12], leading to the discrepancy between the void distribution and damage distribution. In order to identify the formation of voids induced by irradiation or sample preparation, an un-irradiated control sample with twin structures is also measured for comparison, as shown in Fig. 5. It is found that there are no voids observed on both under- and over-focused modes in the un-irradiated control sample. Specifically, there are no voids near the depth of 500 and 2000 nm in the un-irradiated control sample, as presented in Fig. 5c and d (similar to the regions of Fig. 4c and d in the irradiated sample). Therefore, the formation of voids in the irradiated sample can be confirmed to be induced by irradiation.

It can be seen from Fig. 4c and d that the voids distribute apart from the nanotwin boundaries, and no voids can be found outside the two sides of the nanotwin boundaries (The width between the red dashed lines is around 25–30 nm). This trend indicates that nanotwin boundaries can serve as vacancy traps to absorb irradiation-induced vacancies and inhibit the formation of voids around twin boundaries, thus reducing the concentration of voids in the matrix. It is reported that twin boundaries are more stable than other kinds of interfaces, and thus, they are more likely to play an advantageous role acting as sinks for irradiation-induced defects [27,30,62–65]. For example, Meric de Bellefon et al. confirmed the effectiveness of deformation twin boundaries as sinks for point defects in an austenitic stainless steel [27]. The void density is strongly affected and reduced by the presence of deformation twin boundaries, showing an excellent radiation resistance. They found that the swelling rate with deformation twin boundaries in an austenitic stainless steel is 0.09%, which is obviously lower than that (3%) in the austenitic stainless steel without twin boundaries [27].

### 3.3. Dislocation loops and clusters in irradiated and un-irradiated regions

Fig. 6 shows the BF images of dislocations in irradiated and un-irradiated regions. A large number of the dislocation loops and clusters can be found in both irradiated ( $\sim 400 \text{ nm}$ ) and un-irradiated regions ( $\sim 3000 \text{ nm}$ ). The red arrows indicate that dislocation loops exist no matter before or after irradiation. In addition, the density of dislocations seems to be unchanged. The results show that irradiation has not induced obvious variations of dislocations.

### 3.4. Radiation-induced precipitation and segregation

Irradiation usually induces the solutes precipitation or segregation on boundaries or defects. APT was conducted to detect the irradiation-induced nanoscale precipitation. Fig. 7 shows the elemental distributions of Fe, Cr, Ni, Co, and Mn as well as the implanted Au atoms after irradiation from the position of 350 nm of the depth relative to the implanted surface. This depth is corresponding to the position, which possesses the maximum irradiation damage (Fig. 1). It can be seen from Fig. 7 that

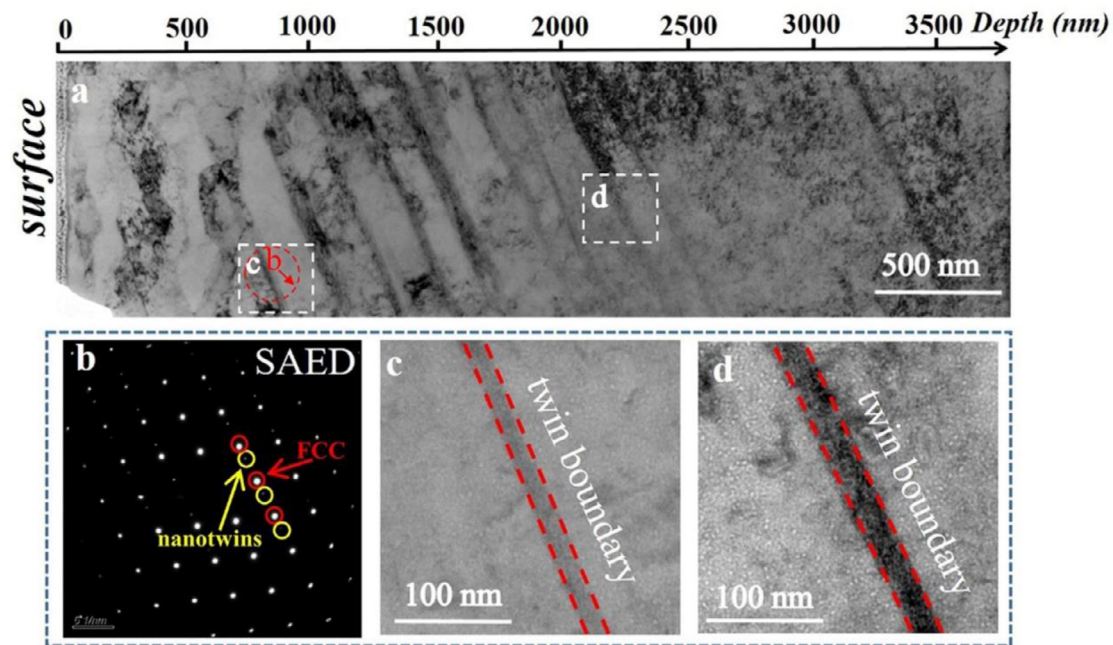


**Fig. 4.** (a) The microstructure of the irradiated HEA along the depth from the surface. (b) The SAED of a nanotwin boundary. (c) and (d) are the under-focused magnifications of corresponding white regions in (a), respectively, showing the voids distribution (For interpretation of the references to color in this figure, the reader is referred to the web version of this article).

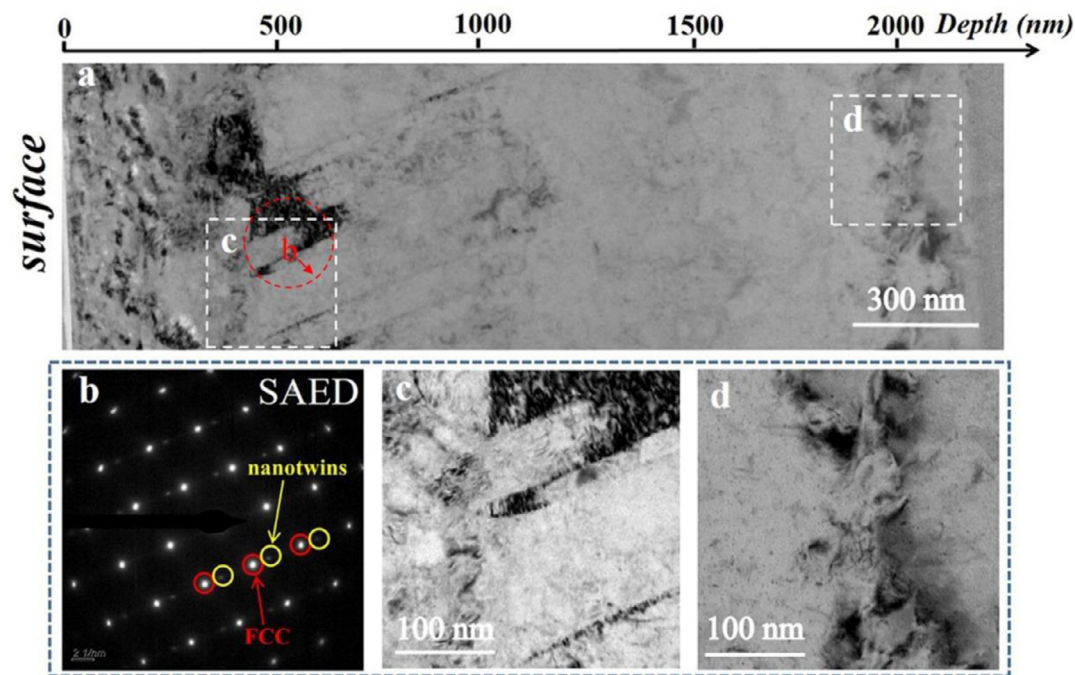


**Fig. 5.** (a) The microstructure of the unirradiated HEA along the depth from the surface. (b) the SAED of the nanotwin boundary. (c) and (d) are the under-focused magnifications of corresponding boxed regions in (a), respectively, showing no voids formation in the un-irradiated counterpart.

all the elements, including the implanted Au atoms, distribute uniformly, indicating that no precipitation occurs under irradiation. The actual composition determined from the APT result is close to the nominal composition. These results confirm that the  $\text{Fe}_{30}\text{Cr}_{25}\text{Ni}_{20}\text{Co}_{15}\text{Mn}_{10}$  HEA exhibits an extraordinary stability of microstructures with a high dose up to 70 dpa.

In order to investigate the RIS behavior, a STEM/EDS line scanning was performed across the nanotwin boundaries. A small scanning step of  $\sim 4$  points/nm was applied to ensure the measurement accuracy. To determine the effect of irradiation on the RIS,

the TEM samples were prepared carefully by FIB to observe a wide region from the sample surface to the depth of  $\sim 3750$  nm (Fig. 8a). As the affected depth by the  $\text{Au}^{2+}$  irradiation is shallower than 1000 nm from the results of the SRIM calculation (Fig. 1), and the voids distribution can reach  $\sim 3000$  nm. Thus, we define zones B and C in Fig. 8a as irradiated and un-irradiated regions. The distributions of Fe, Cr, Ni, Co, and Mn elements around twin boundaries within zones, B and C, are shown in Fig. 8b and c in the same specimen, respectively. From Fig. 8b, Co and Ni are obviously enriched while Fe, Cr, and Mn are depleted on the twin boundary in



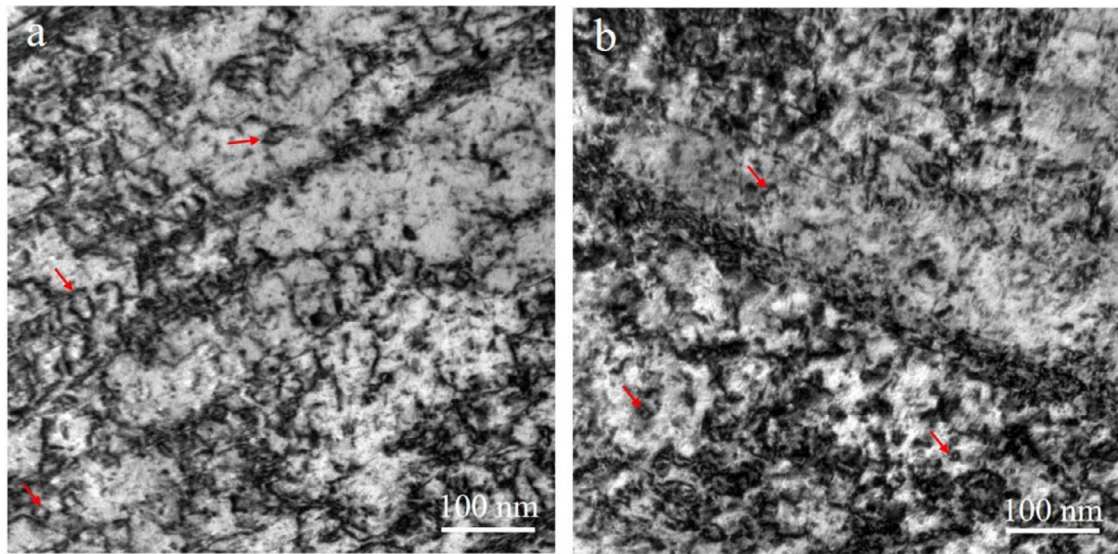


**Fig. 6.** Dislocation loops and clusters in irradiated (a) and un-irradiated regions (b) of BF images with  $g = [200]$ .

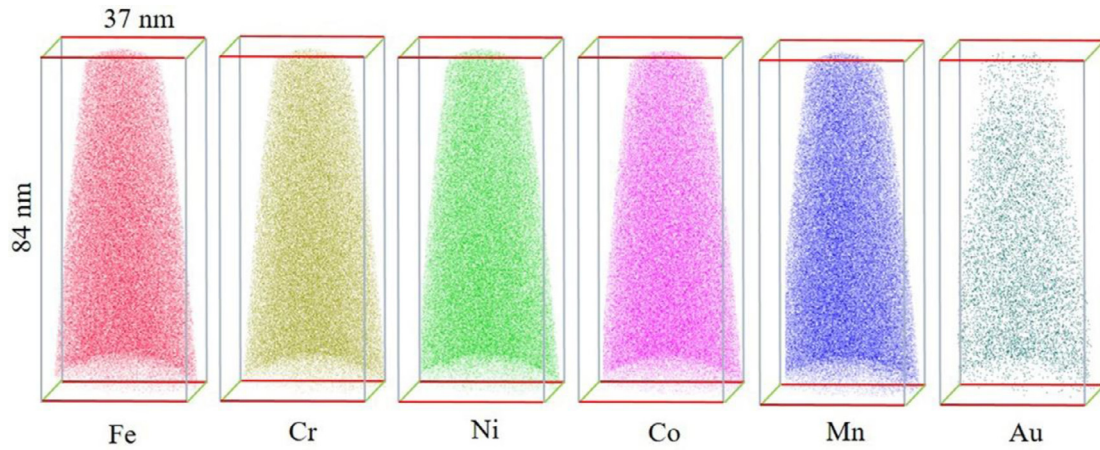


**Fig. 7.** APT maps of the elemental distributions of Fe, Cr, Ni, Co, and Mn as well as the implanted Au atoms upon irradiation.

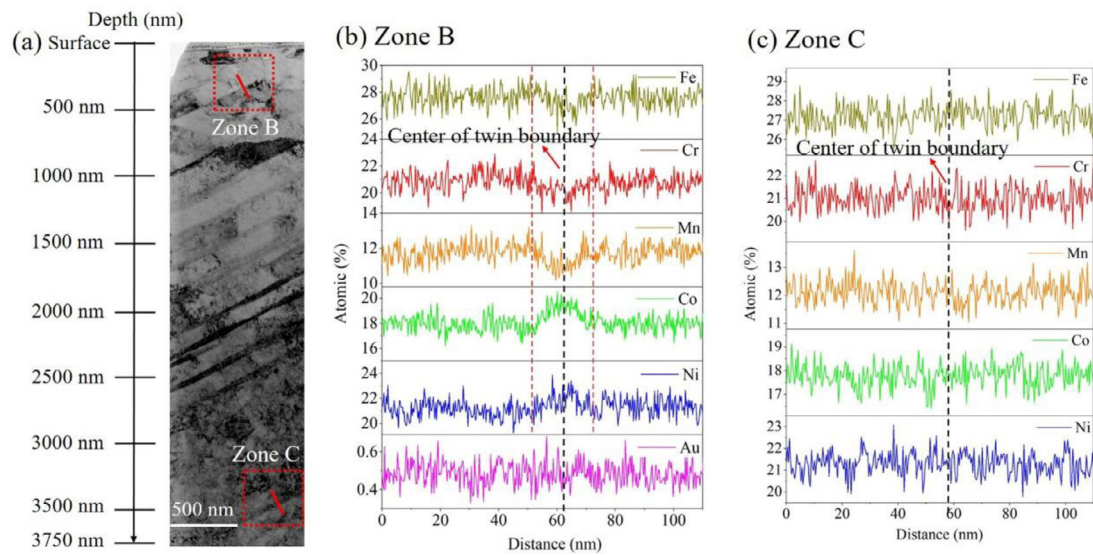


**Fig. 8.** (a) Bright-field TEM image from the surface to 3750 nm containing nanotwin boundaries. The RIS at nanotwin boundaries in (b) irradiated region (zone B in Fig. 8a) and (c) un-irradiated region (zone C in Fig. 8a).

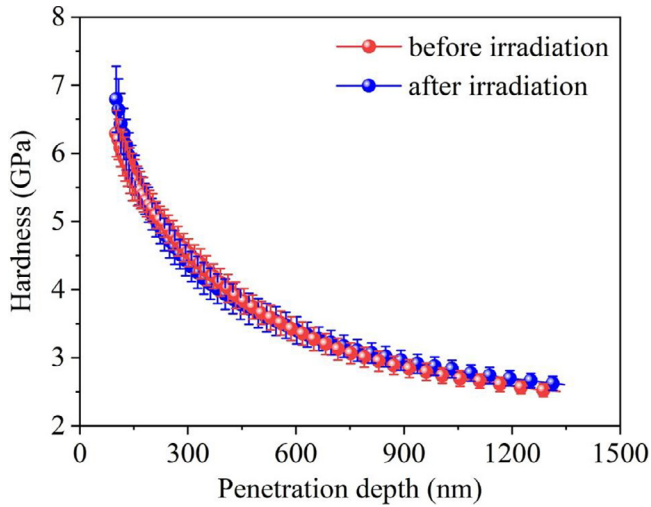


Fig. 9. Hardness variations before and after  $\text{Au}^{2+}$  irradiation.

the irradiated region ( $\sim 350$  nm). There is no apparent segregation of implanted  $\text{Au}^{2+}$  ions. In the un-irradiated region of  $\sim 3500$  nm depth, no elemental segregation is observed around twin boundaries, as presented in Fig. 8c. These results indicate the segregation behavior around the nanotwin boundaries by irradiation.

### 3.5. Evolution of mechanical properties upon irradiation

Nanoindentation was performed to trace the irradiation-induced variation in mechanical properties. The hardness versus depth before and after irradiation is shown in Fig. 9. The data within 100 nm are not shown since the near-surface hardness data exhibit a large scatter due to the surface irregularities [23]. It is clear that the hardness decreases along the depth in both irradiated and un-irradiated samples due to the indentation-size effect [66]. The hardness value after irradiation with a high dose of  $\sim 70$  dpa keeps almost unchanged from Fig. 9. In this study, no precipitation occurs after irradiation as shown in Fig. 7. It is reported that radiation hardening can be attributed to several potential sources: (1) strain/work hardening, (2) void hardening, (3) precipitate hardening and (5) dislocation loop hardening [67]. Among of the above factors, RIP or the formation of dislocation loops usually act as the main obstacles to block the dislocation motion, resulting in the hardening/embrittlement of materials. For example, a model reactor pressure vessel (RPV) steel (known as JRQ) exhibited a 75% increment in hardness due to the Cu precipitation after the  $\text{Fe}^{2+}$  irradiation (1 dpa, 300 °C) [68]. In Fe-12.5at% Cr, the irradiation-induced hardness increase reached 1.0 GPa (28.6%, from 3.5 GPa to 4.5 GPa) at 300 °C with 1 dpa due to the combination of the formation of dislocation loops and the precipitation of  $\alpha'$  particles [69]. Dislocation loops can act as a strong hardening source, and the decrease of its population will lead to the decrease of loop-hardening [11]. Kumar et al. also found that the visible dislocation loops are the main contributors for irradiation induced hardening of HEAs at room temperature irradiation [44]. In Ni-20Fe, the hardening effect induced by the increase of total loop (faulted loops and perfect loops) density is predominant [67]. The contribution to hardness of low density perfect loops of great size and entangled dislocation of networks are much less than the faulted loops and high density of perfect loops [67]. However, no obvious variation of the dislocation before and after irradiation is observed as shown in Fig. 6, indicating that irradiation induced dislocation may not lead to hardening in the HEA.

Hardening caused by dislocation pile-up at the high density grain/twin boundaries can be much greater than the hardening in-

duced by a limited amount of nanovoids and dislocation loops for the for this nanocrystalline alloy. The grain-boundary strengthening can be described as [70]

$$\sigma_y = \sigma_0 + k_y/d^{1/2} \quad (8)$$

where  $\sigma_y$  is the yield stress,  $\sigma_0$  is the lattice friction stress (125 MPa [71]),  $k_y$  is the strengthening coefficient (226  $\text{MPa} \mu\text{m}^{1/2}$  from FeCoNiCrMn system [72]) and  $d$  is the average grain diameter.  $\sigma_y = 160$  MPa is obtained.

The strengthening by nanotwin boundaries can be described as follows [73]:

$$\sigma_y = \sigma_0 + k \left[ \frac{1}{d_{\text{twin}}} + \frac{1}{D} \right]^{\frac{1}{2}} + \alpha G b \sqrt{\rho_d} \quad (9)$$

$d_{\text{twin}}$  is the twin spacing,  $D$  is the crystallite size,  $G$  is the shear modulus (78.5 GPa [46]), and  $b$  is the burger vector,  $\rho_d$  is the dislocation density,  $k$  (226  $\text{MPa} \mu\text{m}^{1/2}$  [72]) and  $\alpha$  (0.2 for FCC metals) is constant. Then we can get  $\sigma_y = 516$  MPa.

For the radiation hardening, only voids are observed in this study. According to Dispersed Barrier Hardening (DBH) model, contributions to hardening of nanoclusters can be described as [74]

$$\Delta\sigma = M\alpha G b \sqrt{dN} \quad (10)$$

where  $M$  is the Taylor factor [46],  $\alpha$  is a constant,  $G$  is the shear modulus of the matrix,  $b$  is the Burgers vector

of gliding dislocations,  $N$  and  $d$  are the number density and mean size of voids, respectively.  $\Delta\sigma$  is calculated to be 125 MPa.

It is found that grain/twin boundary strengthening (hardening) contributes to 676 MPa hardness, while radiation hardening induced by voids is only 125 MPa. Therefore, radiation hardening can be negligible compared to the grain-boundary strengthening (hardening). However, although the voids are observed in this study, no hardening is detected in this study after irradiation, indicating that the small voids may contribute to the hardening. Zhang et al. found that the irradiation-induced small voids have almost no contribution to the hardening, and the main contributor of hardening is the dislocation loop [75]. Jin et al. report that void hardening may not be the primary hardening source, and the dislocation (loops) may play the dominant role [11,39]. The presence of a high number of twin boundaries can effectively capture vacancies and interstitials, restraining the irradiation-induced precipitation and hardening. Therefore, the hardness of the irradiated  $\text{Fe}_{30}\text{Cr}_{25}\text{Ni}_{20}\text{Co}_{15}\text{Mn}_{10}$  HEA remains almost the same as the un-irradiated one.

## 4. Discussion

### 4.1. Effects of defect sinks on the irradiation-induced vacancies and interstitials

To further investigate the effects of defect sinks on the number densities of irradiation-induced vacancies and interstitials, the sink strengths of nanotwin boundaries, grain boundaries, and dislocation networks are evaluated. The sink strength of the dislocation networks,  $S_d$ , is proportional to the dislocation density, which can be estimated as  $\rho_d$  and  $1.2\rho_d$  for the vacancies and interstitials, respectively [76]. Then we can obtain the sink strength of the dislocation net,  $S_d = 4.56 \times 10^{13} \text{ m}^{-2}$  for vacancies, and  $S_d = 5.47 \times 10^{13} \text{ m}^{-2}$  for interstitials. The way for the estimation of sink strengths,  $S_{\text{tw}}$ , of twin boundaries with the thickness  $d_t$ , and grain boundaries with a radius,  $R$ ,  $S_g$  is via the total sink strength ( $S_t$ ) from all the “single crystal” microstructure within the grain [77]:

$$S_{\text{tw}} = \frac{2S_t^{0.5}}{d_t} / \left[ \coth \frac{S_t^{0.5}}{2} d_t - \frac{2}{S_t^{0.5} d_t} \right] \quad (11)$$



$$S_g = S_t \frac{R_{\text{mean}} S_t^{0.5} \coth R_{\text{mean}} S_t^{0.5} - 1}{1 + \frac{S_t R_{\text{mean}}^2}{3} - R_{\text{mean}} S_t^{0.5} \coth R_{\text{mean}} S_t^{0.5}} \quad (12)$$

where  $S_t$  can be estimated as  $S_d$  because the dislocation networks are the single type of defects for the foil and grain [77]. With the twin thicknesses of 11.64  $\mu\text{m}$  and 27 nm for the annealing twins and nanotwins, respectively, the sink strength of annealing twin and nanotwin boundaries for vacancies,  $S_{\text{TW},v}$ , is  $1.16 \times 10^{12} \text{ m}^{-2}$  and  $3.7 \times 10^{13} \text{ m}^{-2}$ , respectively. The sink strength of the annealing twin and nanotwin boundaries for interstitials,  $S_{\text{TW},i}$ , can be estimated as  $1.2 \times 10^{12} \text{ m}^{-2}$  and  $1.65 \times 10^{16} \text{ m}^{-2}$ , respectively. The sink strength of nanotwins for both vacancies and interstitials is higher than those of annealing twins. Similarly, from Eq. (12), we can obtain for grain boundaries with  $R$  of 21  $\mu\text{m}$  (half of the grain size), the sink strength for vacancies and interstitials ( $S_{g,v}$  and  $S_{g,i}$ ) is  $7.88 \times 10^{11} \text{ m}^{-2}$  and  $8.62 \times 10^{11} \text{ m}^{-2}$ , respectively. The sink strength of nanotwin boundaries for vacancies is approximately 50 times larger than that of the grain boundaries and of the same order of dislocation networks. The sink strength of nanotwin boundaries for interstitials is four orders of magnitude larger than that of grain boundaries, and 300 times greater than that of a dislocation networks, indicating that nanotwin boundaries are good sinks for interstitials and thus, inhibit their gathering to form precipitates and dislocations (loops) during irradiation. The high sink strength along with the large volume fraction of the nanotwin boundaries makes them play the main role in the defects absorption.

#### 4.2. Swelling resistance of the HEA upon $\text{Au}^{2+}$ ion irradiation

The swelling phenomena during the irradiation are mainly attributed to the formation of voids. Voids commonly form in the irradiated materials for doses above  $\sim 1$  dpa due to the accumulation of radiation-induced vacancies, specifically for metals and alloys with FCC structures [11]. To investigate the swelling resistance, the voids are analyzed from the surface to the depth of  $\sim 3000$  nm where voids reside. The volume swelling can be estimated as

$$S_v = \frac{\Delta V}{V} = \frac{\frac{\pi}{6} \sum_i d_i^3}{A\delta - \frac{\pi}{6} \sum_i d_i^3} \quad (13)$$

where  $A$  and  $\delta$  are the areas of the characterized region and the thickness of the TEM sample ( $\sim 50$  nm), and  $d$  is the average diameter of the voids [78]. With the determined values from TEM, the volume swelling in this HEA can be calculated as 0.002%/dpa, which is obviously lower than that of Ni-17Mo-7Cr alloy (0.04%/dpa) [79] after being irradiated with 3 MeV  $\text{Au}^{2+}$  at room temperature and Hastelloy N alloy (0.12%/dpa) after 7 and 1 MeV Xe ions irradiations at room temperature [80]. The low swelling can be attributed to two reasons: one is due to the component complexity of HEAs. Multiple types of vacancies and interstitials form under irradiation are unstable due to their high formation energy, large atomic-level stress, and low migration energy [81], promoting the recombination of vacancies and interstitials with the so-called self-healing mechanism. Our HEA possesses the similar self-healing mechanism, as reported in other HEAs. More important, the lower swelling, as compared to the other HEAs, can be contributed from the high volume fraction of twin boundaries, which act as vacancy sinks and hinder the formation of voids.

#### 4.3. RIS resistance of the HEA upon $\text{Au}^{2+}$ -ion irradiation

The magnitude of RIS can be defined as the radiation-induced composition change relative to that of the un-irradiation matrix. The RIS magnitude in  $\text{Fe}_{30}\text{Cr}_{25}\text{Ni}_{20}\text{Co}_{15}\text{Mn}_{10}$  after 70 dpa room temperature ion irradiation is only Fe (3.6%), Cr (4.8%), Mn (8.8%),

Co (8.3%), and Ni (7.1%) in atomic percent as shown in Fig. 8, respectively. The segregation levels of all the elements are very weak and lower than 10%. The RIS behaviors in  $\text{Fe}_{30}\text{Cr}_{25}\text{Ni}_{20}\text{Co}_{15}\text{Mn}_{10}$  can be attributed to the inverse Kirkendall (IK) mechanism. The sequence of elements on the order of the atomic radius,  $R$ , from large to small sizes is: Mn, Cr, Fe, Co, and Ni [82]. We suppose Mn/Cr/Fe as oversized atoms, and Co/Ni as undersized atoms. The oversized atoms have the high mobility and tend to deplete at defect sinks, while the undersized atoms have the low mobility and tend to enrich due to the IK mechanism [82]. The measured result of diffusion coefficients of alloy elements in the FeCrNiCoMn HEA is  $D_{\text{Mn}} > D_{\text{Cr}} > D_{\text{Fe}} > D_{\text{Co}} > D_{\text{Ni}}$  [57,83]. Both the IK effect and diffusion coefficients lead to the same result that Mn/Cr/Fe deplete, and Co/Ni enrich at nanotwin boundaries. Similar RIS behaviors were observed in the CrFeCoNi and FeCrNiCoMn HEAs with Co/Ni enriched and Fe/Cr/Mn depleted at dislocation loops and voids [25,34,84]. However, to our knowledge, the RIS behavior at twin boundaries in HEAs has rarely been reported, while twin boundaries usually exist in the FCC HEAs due to the low stacking fault energy. In general, the solute atoms tend to segregate spontaneously to the defect sinks due to the high energy of sinks. The large number of nanotwin boundaries will preferentially adsorb the point defects, including both vacancies and interstitials [85]. The annihilation of vacancies and interstitials at nanotwin boundaries causes the elemental segregation during irradiation. The low RIS magnitude in  $\text{Fe}_{30}\text{Cr}_{25}\text{Ni}_{20}\text{Co}_{15}\text{Mn}_{10}$  can be attributed to the sluggish diffusion kinetics, as compared to the conventional nuclear materials [44]. The high lattice distortion of HEAs can suppress RIS due to the reduced defect diffusion and the enhanced vacancy/interstitial recombination [25], leading to the slight segregation magnitude at twin boundaries. The insignificant hardening feature, low swelling rate, and weak RIS level indicate that the newly-designed HEA presents an excellent radiation tolerance, and can be a promising candidate material for nuclear reactors.

## 5. Conclusion

In summary, this paper reports the alloy design, preparation, and irradiation tolerance of the  $\text{Fe}_{30}\text{Cr}_{25}\text{Ni}_{20}\text{Co}_{15}\text{Mn}_{10}$  HEA. The following conclusions can be drawn:

- (1) The  $\text{Fe}_{30}\text{Cr}_{25}\text{Ni}_{20}\text{Co}_{15}\text{Mn}_{10}$  HEA presents a high ion-irradiation stability. There is no nanoscale precipitation and irradiation-induced hardening at a high dose irradiation ( $\sim 70$  dpa).
- (2) The nanotwin boundaries have a higher sink strength for vacancies than grain boundaries and dislocation network, which are beneficial to absorb more irradiation-induced vacancies on the nanotwin boundaries, inhibiting the formation of voids inside the grains.
- (3) The sink strengths of nanotwin boundaries for interstitials are also larger than those of grain boundaries and dislocation networks, indicating that nanotwin boundaries are good sinks for interstitials and inhibit their gathering to form precipitates and dislocations (loops) during irradiation.
- (4) The swelling rate is as low as 0.002%/dpa. This low swelling rate can be attributed to the combination of the self-healing mechanism and the existence of high fractions of nanotwin boundaries, which act as effective vacancy sinks.
- (5) RIS is observed at nanotwin boundaries with the oversized Mn/Fe/Cr depletion and undersized Co/Ni enrichment due to the inverse Kirkendall mechanism. The magnitude of RIS of all the elements in the  $\text{Fe}_{30}\text{Cr}_{25}\text{Ni}_{20}\text{Co}_{15}\text{Mn}_{10}$  HEA is very weak and lower than 10%.



## Declaration of Competing Interest

The authors declare the following financial interests/personal relationships which may be considered as potential competing interests:

## CRediT authorship contribution statement

**Y. Zhang:** Conceptualization, Investigation, Visualization, Writing – original draft, Funding acquisition. **W.Q. Jiang:** Investigation, Data curation, Visualization. **A. Gokhman:** Validation, Formal analysis. **J.J. Yang:** Validation. **K. Shi:** Validation. **J.H. Luan:** Validation. **Y. Cui:** Writing – review & editing, Funding acquisition. **Peter K Liaw:** Funding acquisition, Writing – review & editing. **C.T. Liu:** Writing – review & editing. **Z.W. Zhang:** Conceptualization, Writing – review & editing, Funding acquisition.

## Acknowledgments

The present work is supported by the National Key Research and Development Project (Grant No. 2018YFE0115800), Youth Talent Project of China National Nuclear Corporation (Grant No. CNNC2019YTEP-HEU01), the [Fundamental Research Funds for the Central Universities](#) (Grant No. 3072020CFT1005), the NSFC Funding (Grant Nos. 52001083, 11874327, 51701051), China Postdoctoral Science Foundation Funded Project (Grant No. 2019T120255), [Natural Science Foundation of Heilongjiang](#) (Grant No. LH2019E030), Innovation Center of Nuclear Materials for National Defense Industry (HCL-08), Fund project (SKLMEA-K201902) from State Key Laboratory of Metal Material for Marine Equipment and Application and Heilongjiang Touyan Innovation Team Program. The atom probe tomography research was conducted at the Inter-University 3D Atom Probe Tomography Unit of City University of Hong Kong supported by the CityU grant, 9360161, and Collaborative Research Fund (CRF) grant, C1027-14E. PKL is very grateful to the support of (1) the National Science Foundation (DMR-1611180 and 1809640) with the program directors, Drs. Judith Yang, Gary Shiflet, and Diana Farkas and (2) the U.S. Army Office Project (W911NF-13-1-0438 and W911NF-19-2-0049) with the program managers, Drs. Michael P. Bakas, David M. Stepp, and S. Mathaudhu.

## References

- [1] S.J. Zinkle, G.S. Was, Materials challenges in nuclear energy, *Acta Mater.* 61 (2013) 735–758.
- [2] F. Granberg, K. Nordlund, M.W. Ullah, K. Jin, C. Lu, H. Bei, L.M. Wang, F. Djurabekova, W.J. Weber, Y. Zhang, Mechanism of radiation damage reduction in equiatomic multicomponent single phase alloys, *Phys. Rev. Lett.* 116 (2016) 135504.
- [3] B. Cantor, I.T.H. Chang, P. Knight, A.J.B. Vincent, Microstructural development in equiatomic multicomponent alloys, *Mater. Sci. Eng. A* 375–377 (2004) 213–218.
- [4] Y. Zhang, T.T. Zuo, Z. Tang, M.C. Gao, K.A. Dahmen, P.K. Liaw, Z.P. Lu, Microstructures and properties of high-entropy alloys, *Prog. Mater. Sci.* 61 (2014) 1–93.
- [5] J.W. Yeh, S.K. Chen, S.J. Lin, J.Y. Gan, T.S. Chin, T.T. Shun, C.H. Tsau, S.Y. Chang, Nanostructured high-entropy alloys with multiple principal elements: novel alloy design concepts and outcomes, *Adv. Eng. Mater.* 6 (2004) 299–303.
- [6] D.B. Miracle, O.N. Senkov, A critical review of high entropy alloys and related concepts, *Acta Mater.* 122 (2017) 448–511.
- [7] Y. Lu, H. Huang, X. Gao, C. Ren, J. Gao, H. Zhang, S. Zheng, Q. Jin, Y. Zhao, C. Lu, T. Wang, T. Li, A promising new class of irradiation tolerant materials:  $\text{Ti}_2\text{ZrHf}_{0.5}\text{Mo}_{0.2}$  high-entropy alloy, *J. Mater. Sci. Technol.* 35 (2019) 369–373.
- [8] D.S. Aidhy, C. Lu, K. Jin, H. Bei, Y. Zhang, L. Wang, W.J. Weber, Point defect evolution in Ni, NiFe and NiCr alloys from atomistic simulations and irradiation experiments, *Acta Mater.* 99 (2015) 69–76.
- [9] S. Xia, M.C. Gao, T. Yang, P.K. Liaw, Y. Zhang, Phase stability and microstructures of high entropy alloys ion irradiated to high doses, *J. Nucl. Mater.* 480 (2016) 100–108.
- [10] W. Zhang, P.K. Liaw, Y. Zhang, Science and technology in high-entropy alloys, *Sci. China Mater.* 61 (2018) 2–22.
- [11] K. Jin, C. Lu, L.M. Wang, J. Qu, W.J. Weber, Y. Zhang, H. Bei, Effects of compositional complexity on the ion-irradiation induced swelling and hardening in Ni-containing equiatomic alloys, *Scr. Mater.* 119 (2016) 65–70.
- [12] C. Lu, L. Niu, N. Chen, K. Jin, T. Yang, P. Xiu, Y. Zhang, F. Gao, H. Bei, S. Shi, M.R. He, I.M. Robertson, W.J. Weber, L. Wang, Enhancing radiation tolerance by controlling defect mobility and migration pathways in multicomponent single-phase alloys, *Nat. Commun.* 7 (2016) 13564.
- [13] S.Q. Xia, X. Yang, T.F. Yang, S. Liu, Y. Zhang, Irradiation resistance in  $\text{Al}_x\text{CoCrFeNi}$  high entropy alloys, *JOM* 67 (2015) 2340–2344.
- [14] T. Yang, S. Xia, S. Liu, C. Wang, S. Liu, Y. Fang, Y. Zhang, J. Xue, S. Yan, Y. Wang, Precipitation behavior of  $\text{Al}_x\text{CoCrFeNi}$  high entropy alloys under ion irradiation, *Sci. Rep.* 6 (2016) 32146.
- [15] A.J. Ardell, P. Bellon, Radiation-induced solute segregation in metallic alloys, *Curr. Opin. Solid State Mater. Sci.* 20 (2016) 115–139.
- [16] F. Soisson, Kinetic Monte Carlo simulations of radiation induced segregation and precipitation, *J. Nucl. Mater.* 349 (2006) 235–250.
- [17] N. Almirall, P.B. Wells, T. Yamamoto, K. Wilford, T. Williams, N. Riddle, G.R. Odette, Precipitation and hardening in irradiated low alloy steels with a wide range of Ni and Mn compositions, *Acta Mater.* 179 (2019) 119–128.
- [18] G.R. Odette, M.J. Alinger, B.D. Wirth, Recent developments in irradiation resistant steels, *Annu. Rev. Mater. Res.* 38 (2008) 471e503.
- [19] N. Almirall, P.B. Wells, S. Pal, P.D. Edmondson, T. Yamamoto, K. Murakami, G.R. Odette, The mechanistic implications of the high temperature, long time thermal stability of nanoscale Mn-Ni-Si precipitates in irradiated reactor pressure vessel steels, *Scr. Mater.* 181 (2020) 134–139.
- [20] Z. Jiao, G.S. Was, Novel features of radiation-induced segregation and radiation-induced precipitation in austenitic stainless steels, *Acta Mater.* 59 (2011) 1220e1238.
- [21] S. Shu, B.D. Wirth, P.B. Wells, D.D. Morgan, G.R. Odette, Multi-technique characterization of the precipitates in thermally aged and neutron irradiated Fe-Cu and Fe-Cu-Mn model alloys: atom probe tomography reconstruction implications, *Acta Mater.* 146 (2018) 237–252.
- [22] N. Baluc, P. Spätig, M. Victoria, On the potentiality of using ferritic/martensitic steels as structural materials for fusion reactors, *Nucl. Fusion* 44 (2004) 56.
- [23] G.R. Odette, T. Yamamoto, T.J. Williams, R.K. Nanstad, C.A. English, On the history and status of reactor pressure vessel steel ductile to brittle transition temperature shift prediction models, *J. Nucl. Mater.* 526 (2019) 151863.
- [24] D.J. Sprouster, J. Sinheimer, E. Dooryhee, S.K. Ghose, P. Wells, T. Stan, N. Almirall, G.R. Odette, L.E. Ecker, Structural characterization of nanoscale intermetallic precipitates in highly neutron irradiated reactor pressure vessel steels, *Scr. Mater.* 113 (2016) 18–22.
- [25] C. Lu, T. Yang, K. Jin, N. Gao, P. Xiu, Y. Zhang, F. Gao, H. Bei, W.J. Weber, K. Sun, Y. Dong, L. Wang, Radiation-induced segregation on defect clusters in single-phase concentrated solid-solution alloys, *Acta Mater.* 127 (2017) 98–107.
- [26] C.M. Barr, J.E. Nathaniel, K.A. Unocic, J. Liu, Y. Zhang, Y. Wang, M.L. Taheri, Exploring radiation induced segregation mechanisms at grain boundaries in equiatomic  $\text{CoCrFeNiMn}$  high entropy alloy under heavy ion irradiation, *Scr. Mater.* 156 (2018) 80–84.
- [27] G. Meric de Bellefon, I.M. Robertson, T.R. Allen, J.C. van Duysen, K. Sridharan, Radiation-resistant nanotwinned austenitic stainless steel, *Scr. Mater.* 159 (2019) 123–127.
- [28] J. Li, D.Y. Xie, S. Xue, C. Fan, Y. Chen, H. Wang, J. Wang, X. Zhang, Superior twin stability and radiation resistance of nanotwinned Ag solid solution alloy, *Acta Mater.* 151 (2018) 395–405.
- [29] C.M. Barr, K.A. Unocic, K. Hattar, X.M. Bai, M.L. Taheri, Anisotropic radiation-induced segregation in 316L austenitic stainless steel with grain boundary character, *Acta Mater.* 67 (2014) 145–155.
- [30] J. Ding, S. Yang, B. Zhu, H. Liu, G. Liu, L. Zhou, Q. Zhan, F. Wan, Twins induced by high-temperature ion irradiation in body-centered cubic V-4Cr-4Ti alloy, *Scr. Mater.* 162 (2019) 377–381.
- [31] K.Y. Yu, C. Sun, Y. Liu, H. Wang, M.A. Kirk, M. Li, X. Zhang, Removal of stacking-fault tetrahedra by twin boundaries in nanotwinned metals, *Nat. Commun.* 4 (2013) 1377.
- [32] K.Y. Yu, F. Khatkhatay, H. Wang, M.A. Kirk, X. Zhang, *In situ* studies of irradiation-induced twin boundary migration in nanotwinned Ag, *Scr. Mater.* 69 (2013) 385–388.
- [33] F. He, Z. Wang, Q. Wu, D. Chen, T. Yang, J. Li, J. Wang, C.T. Liu, J.J. Kai, Tuning the defects in face centered cubic high entropy alloy via temperature-dependent stacking fault energy, *Scr. Mater.* 155 (2018) 134–138.
- [34] M.R. He, S. Wang, S. Shi, K. Jin, H. Bei, K. Yasuda, S. Matsumura, K. Higashida, I.M. Robertson, Mechanisms of radiation-induced segregation in Cr-FeCoNi-based single-phase concentrated solid solution alloys, *Acta Mater.* 126 (2017) 182–193.
- [35] S. Huang, W. Li, S. Lu, F. Tian, J. Shen, E. Holmström, L. Vitos, Temperature dependent stacking fault energy of FeCrCoNiMn high entropy alloy, *Scr. Mater.* 108 (2015) 44–47.
- [36] Z. Li, S. Zhao, S.M. Alotaibi, Y. Liu, B. Wang, M.A. Meyers, Adiabatic shear localization in the CrMnFeCoNi high-entropy alloy, *Acta Mater.* 151 (2018) 424–431.
- [37] S.F. Liu, Y. Wu, H.T. Wang, J.Y. He, J.B. Liu, C.X. Chen, X.J. Liu, H. Wang, Z.P. Lu, Stacking fault energy of face-centered-cubic high entropy alloys, *Intermetallics* 93 (2018) 269–273.
- [38] Z. Wu, H. Bei, G.M. Pharr, E.P. George, Temperature dependence of the mechanical properties of equiatomic solid solution alloys with face-centered cubic crystal structures, *Acta Mater.* 81 (2014) 428–441.
- [39] K. Jin, W. Guo, C. Lu, M.W. Ullah, Y. Zhang, W.J. Weber, L. Wang, J.D. Poplawsky, H. Bei, Effects of Fe concentration on the ion-irradiation induced defect evolution and hardening in Ni-Fe solid solution alloys, *Acta Mater.* 121 (2016) 365–373.

- [40] B.C. De Cooman, Y. Estrin, S.K. Kim, Twinning-induced plasticity (TWIP) steels, *Acta Mater.* 142 (2018) 283–362.
- [41] S.J. Lee, H. Fujii, K. Ushioda, Thermodynamic calculation of the stacking fault energy in Fe–Cr–Mn–C–N steels, *J. Alloy. Compd.* 749 (2018) 776–782.
- [42] J.C. Li, Q. Jiang, Stacking fault energy of iron-base shape memory alloys, *Mater. Lett.* 38 (1999) 275–277.
- [43] L. Yang, H. Ge, J. Zhang, T. Xiong, Q. Jin, Y. Zhou, X. Shao, B. Zhang, Z. Zhu, S. Zheng, X. Ma, High He-ion irradiation resistance of CrMnFeCoNi high-entropy alloy revealed by comparison study with Ni and 304SS, *J. Mater. Sci. Technol.* 35 (2019) 300–305.
- [44] N.A.P.K. Kumar, C. Li, K.J. Leonard, H. Bei, S.J. Zinkle, Microstructural stability and mechanical behavior of FeNiMnCr high entropy alloy under ion irradiation, *Acta Mater.* 113 (2016) 230–244.
- [45] S.S. Xu, Y. Zhao, D. Chen, L.W. Sun, L. Chen, X. Tong, C.T. Liu, Z.W. Zhang, Nanoscale precipitation and its influence on strengthening mechanisms in an ultra-high strength low-carbon steel, *Int. J. Plast.* 128 (2020) 102677.
- [46] J.Y. He, H.L. Huang, X.D. Xu, M.W. Chen, Y. Wu, X.J. Liu, T.G. Nieh, K. An, Z.P. Lu, A precipitation-hardened high-entropy alloy with outstanding tensile properties, *Acta Mater.* 10 (2016) 187–196.
- [47] P. Thirathipviwat, J. Jayaraj, J. Bednarcik, H. Wendrock, T. Gemming, J. Freudenberger, K. Nielsch, J. Han, A comparison study of dislocation density, recrystallization and grain growth among nickel, FeNiCo ternary alloy and FeNiCoCrMn high entropy alloy, *J. Alloy. Compd.* 790 (2019) 266e273.
- [48] R.E. Stoller, M.B. Toloczko, G.S. Was, A.G. Certain, S. Dwaraknath, F.A. Garner, On the use of SRIM for computing radiation damage exposure, *Nucl. Instrum. Methods B* 310 (2013) 75–80.
- [49] Y. Iwamoto, M. Harada, K. Niita, Calculation of displacement cross-sections for structural materials in accelerators using PHITS event generator and its applications to radiation damage, *J. Nucl. Sci. Technol.* 51 (2014) 98–107.
- [50] T.N. Yang, G.H. Velisa, K. Jin, P.Y. Xiu, Y.W. Zhang, H.B. Bei, L.M. Wang, Influence of irradiation temperature on void swelling in NiCoFeCrMn and NiCoFeCrPd, *Scr. Mater.* 158 (2018) 57–61.
- [51] C.M. Parish, K.G. Field, A.G. Certain, J.P. Wharry, Application of STEM characterization for investigating radiation effects in BCC Fe-based alloys, *J. Mater. Res.* 30 (2015) 1275–1289.
- [52] J.W. Christian, S. Mahajan, Deformation twinning, *Prog. Mater. Sci.* 39 (1995) 1–157.
- [53] A. Ghaderi, M.R. Barnett, Sensitivity of deformation twinning to grain size in titanium and magnesium, *Acta Mater.* 59 (2011) 7824–7839.
- [54] M.R. Barnett, A. Ghaderi, Yield point elongation due to twinning in a magnesium alloy, *Acta Mater.* 60 (2012) 1433–1443.
- [55] M.R. Barnett, M.D. Nave, A. Ghaderi, Yield point elongation due to twinning in a magnesium alloy, *Acta Mater.* 60 (2012) 1433–1443.
- [56] J. Da browa, G. Cieslak, T. Kulik, M. Danielewski, J.W. Yeh, Interdiffusion in the FCC-structured Al–Co–Cr–Fe–Ni high entropy alloys: experimental studies and numerical simulations, *J. Alloy. Compd.* 674 (2016) 455–462.
- [57] K.Y. Tsai, M.H. Tsai, J.W. Yeh, Sluggish diffusion in Co–Cr–Fe–Mn–Ni high-entropy alloys, *Acta Mater.* 61 (2013) 4887–4897.
- [58] M. Vaidya, B.S. Murty, G. Wilde, S.V. Divinski, Bulk tracer diffusion in CoCrFeNi and CoCrFeMnNi high entropy alloys, *Acta Mater.* 146 (2018) 211–224.
- [59] A. Mehta, Y.H. Sohn, Investigation of sluggish diffusion in FCC Al<sub>0.25</sub>CoCrFeNi high-entropy alloy, *Mater. Res. Lett.* 9 (2021) 239–246.
- [60] T.N. Yang, G.H. Velisa, K. Jin, P.Y. Xiu, M.L. Crespiello, Y.W. Zhang, H.B. Bei, L.M. Wang, Effect of alloying elements on defect evolution in Ni–20X binary alloys, *Acta Mater.* 151 (2018) 159–168.
- [61] C.Y. Lu, K. Jin, G.H. Velisa, P.Y. Xiu, M. Song, Q. Peng, F. Gao, Y.W. Zhang, H.B. Bei, W.J. Weber, L.M. Wang, Enhanced void swelling in NiCoFeCrPd high-entropy alloy by indentation-induced dislocations, *Mater. Res. Lett.* 6 (2018) 584–591.
- [62] C.M. Barr, L. Barnard, J.E. Nathaniel, K. Hattar, K.A. Unocic, I. Szlurfska, D. Morgan, M.L. Taheri, Grain boundary character dependence of radiation-induced segregation in a model Ni–Cr alloy, *J. Mater. Res.* 30 (2015) 1290–1299.
- [63] J.L. Brimhall, B. Mastel, Enhanced neutron radiation damage at twin boundaries, *J. Appl. Phys.* 38 (1967) 3027–3028.
- [64] H.H. Jin, G.G. Lee, J. Kwon, S.S. Hwang, C. Shin, The formation of radiation-induced segregation at twin bands in ion-irradiated austenitic stainless steel, *J. Nucl. Mater.* 454 (2014) 28–36.
- [65] P. Ahmedabadi, K. Arora, I. Samajdar, S.C. Sharma, P. Bhagwat, Radiation-induced segregation in desensitized type 304 austenitic stainless steel, *J. Nucl. Mater.* 416 (2011) 335–344.
- [66] M. Saleh, A. Xu, C. Hurt, M. Ionescu, J. Daniels, P. Munroe, L. Edwards, D. Bhattacharyya, Oblique cross-section nanoindentation for determining the hardness change in ion-irradiated steel, *Int. J. Plast.* 112 (2019) 242–256.
- [67] P.Y. Xiu, L. Jiang, G.H. Velisa, Y. Tong, H.B. Bei, W.J. Weber, Y.W. Zhang, L.M. Wang, Dislocation loop evolution and radiation hardening in nickel-based concentrated solid solution alloys, *J. Nucl. Mater.* 538 (2020) 152247.
- [68] S. Pecko, C. Heintze, F. Bergner, W. Anwand, V. Slugeň, Fe<sup>2+</sup> ion irradiated JRO steel investigated by nanoindentation and slow-positron doppler broadening spectroscopy, *Nucl. Instrum. Method* 415 (2018) 1–8.
- [69] C. Heintze, F. Bergner, M. Hernández-Mayoral, Ion-irradiation-induced damage in Fe–Cr alloys characterized by nanoindentation, *J. Nucl. Mater.* 417 (2011) 980–983.
- [70] E.O. Hall, The deformation and ageing of mild steel: III discussion of results, *Proc. Phys. Soc. Sect. B* 64 (1951) 747–753.
- [71] F. Otto, Ch. Somsen, H. Bei, G. Eggeler, E.P. George, The influences of temperature and microstructure on the tensile properties of a CoCrFeMnNi high-entropy alloy, *Acta Mater.* 61 (2013) 5743–5755.
- [72] W.H. Liu, J.Y. He, T.G. Nieh, Z.P. Lu, Grain growth and the hall-petch relationship in a high-entropy FeCrNiCoMn alloy, *Scr. Mater.* 68 (2013) 526–529.
- [73] G.H. Xiao, N.R. Tao, K. Lu, Strength–ductility combination of nanostructured Cu–Zn alloy with nanotwin bundles, *Scr. Mater.* 65 (2011) 119–122.
- [74] O. El-Atwani, E. Esquivel, M. Efe, M.R. Chancey, Y.Q. Wang, S.A. Maloy, N. Mara, Nanohardness measurements of heavy ion irradiated coarse- and nanocrystalline-grained tungsten at room and high temperature, *J. Nucl. Mater.* 509 (2018) 276–284.
- [75] Z.X. Zhang, D.S. Chen, W.T. Han, A. Kimura, Irradiation hardening in pure tungsten before and after recrystallization, *Fusion Eng. Des.* 98–99 (2015) 2103–2107.
- [76] A. Hardouin Duparc, C. Moingeon, N. Smetniansky-de-Grande, A. Barbu, Microstructure modeling of ferritic alloys under high flux 1 MeV electron irradiations, *J. Nucl. Mater.* 302 (2002) 413–155.
- [77] R. Bullock, M.R. Hayns, M.H. Wood, Sink strengths for thin film surfaces and grain boundaries, *J. Nucl. Mater.* 90 (1980) 44–59.
- [78] Z. Fan, T. Yang, B. Kombaiah, X. Wang, P.D. Edmondson, Y.W. Zhang, From suppressed void growth to significant void swelling in NiCoFeCr complex concentrated solid-solution alloy, *Materialia* 9 (2020) 100603.
- [79] P. Guo, L. Yan, Q. Huang, Z.J. Li, P. Huai, X.T. Zhou, Irradiation effects in Ni–17Mo–7Cr alloy bombarded with MeV Au ions, *Acta Metall. Sin. (Engl. Lett.)* 28 (2015) 903–908.
- [80] S.J. Zhang, H.C. Chen, G.H. Lei, H.F. Huang, W. Zhang, C.B. Wang, L. Yan, D.J. Fu, M. Tang, Ion irradiation-induced swelling and hardening effect of Hastelloy N alloy, *J. Nucl. Mater.* 489 (2017) 180–186.
- [81] S.Q. Xia, Z. Wang, T.F. Yang, Y. Zhang, Irradiation behavior in high entropy alloys, *J. Iron Steel Res. Int.* 22 (2015) 879–884.
- [82] S. Sun, N. Qiu, K. Zhang, P. He, Y. Ma, F. Gou, Y. Wang, Segregation of Al<sub>1.5</sub>CrFeNi high entropy alloys induced by vacancy-type defects, *Scr. Mater.* 161 (2019) 40–43.
- [83] A. Paul, Comments on “Sluggish diffusion in Co–Cr–Fe–Mn–Ni high-entropy alloys” by K.Y. Tsai, M.H. Tsai and J.W. Yeh, *Acta Mater.* 61 (2013) 4887–4897, *Scr. Mater.* 135 (2017) 153–157.
- [84] T. Yang, S. Xia, W. Guo, R. Hu, J.D. Poplawsky, G. Sha, Y. Fang, Z. Yan, C. Wang, C. Li, Y. Zhang, S.J. Zinkle, Y. Wang, Effects of temperature on the irradiation responses of Al<sub>0.1</sub>CoCrFeNi high entropy alloy, *Scr. Mater.* 144 (2018) 31–35.
- [85] P. Ahmedabadi, V. Kain, K. Arora, I. Samajdar, S.C. Sharma, S. Ravindra, P. Bhagwat, Radiation-induced segregation in austenitic stainless steel type 304: effect of high fraction of twin boundaries, *Mater. Sci. Eng. A* 528 (2011) 7541–7551.